Journal of
**Synchrotron Radiation**

ISSN 0909-0495

Received 19 July 2012
Accepted 25 October 2012

# High-resolution high-efficiency X-ray imaging system based on the in-line Bragg magnifier and the Medipix detector

**Patrik Vagovič,[a]* Dušan Korytár,[b] Angelica Cecilia,[a,c] Elias Hamann,[a,c] Libor Švéda,[d] Daniele Pelliccia,[e] Jürgen Härtwig,[f] Zdenko Zápražný,[b] Peter Oberta,[g,h] Igor Dolbnya,[i] Kawal Shawney,[i] Uwe Fleschig,[j] Michael Fiederle[c] and Tilo Baumbach[a]**

[a]ANKA Light Source, Karlsruhe Institute of Technology, Karlsruhe, Germany, [b]Institute for Electrical Engineering, Slovak Academy of Sciences, Bratislava, Slovakia, [c]FMF, Freiburg, Germany, [d]FNSPE CTU in Prague, Czech Republic, [e]School of Physics, Monash University, Victoria 3800, Australia, [f]ESRF, Grenoble, France, [g]Academy of Sciences of the Czech Republic, Prague, Czech Republic, [h]Rigaku Innovative Technologies Europe, Prague, Czech Republic, [i]Diamond Light Source, UK, and [j]Swiss Light Source, PSI, Switzerland. E-mail: patrik@tagen.tohoku.ac.jp

The performance of a recently developed full-field X-ray micro-imaging system based on an in-line Bragg magnifier is reported. The system is composed of quasi-channel-cut crystals in combination with a Medipix single-photon-counting detector. A theoretical and experimental study of the imaging performance of the crystals–detector combination and a comparison with a standard indirect detector typically used in high-resolution X-ray imaging schemes are reported. The spatial resolution attained by our system is about 0.75 μm, limited only by the current magnification. Compared with an indirect detector system, this system features a better efficiency, signal-to-noise ratio and spatial resolution. The optimal working resolution range of this system is between ∼0.4 μm and 1 μm, filling the gap between transmission X-ray microscopes and indirect detectors. Applications for coherent full-field imaging of weakly absorbing samples are shown and discussed.



**Keywords: Bragg magnifier; germanium; holography; high resolution; in-line; X-ray imaging.**

## 1. Introduction

Hard X-ray methods with sub-micrometer spatial resolution are currently utilized in modern synchrotron facilities and, in selected cases, with laboratory sources. Typically one can use a configuration with parallel X-ray beam and high-resolution detector or X-ray magnification in projection geometry. The former is commonly a synchrotron technique while the latter, mainly implemented in laboratory set-ups, is generally limited by the size of the source (typically a few micrometers). On the other hand, established high-resolution X-ray detecting systems are based on the combination of scintillating screens, diffraction-limited optical microscopes and CCD or CMOS cameras, called indirect detectors (Bonse & Bush, 1996). Typical resolution is slightly above 1 μm, obtainable by magnifying the converted visible light. The need for resolution implies that the scintillating screen must be thin enough to avoid spreading the (incoherent) scintillating process over a large volume. Therefore such conversion is particularly inefficient for hard X-rays, where more than 60% of the usable signal is lost (Cecilia *et al.*, 2011).

Detector limitations can be easily overcome by magnifying the X-ray beam prior to a detector. In this way both resolution and sensitivity of X-ray imaging systems can be improved, by employing magnifying optics such as Fresnel zone plates (Baez, 1960), refractive X-ray lenses (Suehiro *et al.*, 1991), curved mirrors in crossed configuration (Kirkpatrick–Baez, KB) (Kirkpatrick & Baez, 1948) or X-ray waveguides (Pelliccia *et al.*, 2010). Where the objective lens is placed after the sample, high resolution has been demonstrated in a full-field configuration. Another approach, which does not need a high-resolution objective lens, consists of the use of a Bragg magnifying optics (Boetinger *et al.*, 1979; Kagoshima *et al.*, 2000; Kobayashi *et al.*, 2001; Spal, 2001; Stampanoni *et al.*, 2002; Schäfer & Köhler, 2003; Vagovič *et al.*, 2011). The advantage of such an approach is to keep the X-ray beam divergence very low, so the effective source size does not play a significant role, as in cone-beam laboratory imaging set-ups. The Bragg magnifier can be placed in front of or behind the sample. In the former case, the divergence decrease provides, after the magnifier, a quasi-parallel larger beam illumination to the sample. The latter case, which is the subject of the

present study, corresponds to a magnification of the sample projected image. The image is then recorded by a sensitive moderate-resolution X-ray detector such as the single-photon-counting detector Medipix (Llopart *et al.*, 2002).

The combination of a single-photon-counting detector (PILATUS) with silicon-based Bragg magnifier was first demonstrated by Stampanoni *et al.* (2006). In this work, besides the novelty of the approach, the obtainable image quality was far from being of practical use because of strong geometrical deformations and the very small field of view. This was due to very high magnification obtained with a single reflection, in conjunction with a low-spatial-resolution detector such as PILATUS (172 µm pixel size).

In this work we demonstrate the performance of a full-field micro-imaging system based on an in-line germanium Bragg magnifier composed of two identical quasi-channel-cut crystals in combination with the single-photon-counting detector Medipix (BMM). With this approach it is not necessary to produce extremely high magnification with a single crystal; therefore, the requirements for the crystal surface quality are less stringent, yet the total magnification can be extremely high. Furthermore, the combination of two crystals in the $(+n, -n)$ configuration leads to an in-line set-up which is technically more convenient compared with Bragg magnifiers composed only of a single crystal (magnifying in one direction). We present the description of the device, design parameters and the experimental results obtained on beamline B16 (Sawhney *et al.*, 2010) at Diamond Light Source (Oxford, UK), the Optics beamline at the Swiss Light Source (Villigen, Switzerland) and ANKA light source (Karlsruhe, Germany). We confront, both qualitatively and quantitatively, the imaging performances of the BMM with an indirect detector with comparable resolution. Finally we address the capability of our set-up for coherent full-field imaging schemes.

## 2. Description of the device

The Bragg magnifier scheme introduced by Vagovič *et al.* (2011) demonstrated the possibility of performing high-resolution imaging with a pair of crossed monolithic channel-cut crystals. This configuration is clearly favorable in terms of easy alignment procedures. Nevertheless, a major limitation has been identified. In order to build a two-dimensional system, two channel-cut crystals have to be employed. It is extremely difficult to have *exactly* the same magnification (*i.e.* the same asymmetry angles) for the two monolithic pieces and therefore the magnification factor is usually different for the two directions. If we consider in addition that the surface quality of a channel-cut crystal is worse than the surface quality of a flat crystal, we understand that such a set-up is prone to distortions and aberrations when high magnification is to be achieved. Therefore such a configuration was not able to reach an aberration-free sub-micrometer resolution with a Medipix detector. Based on this experience we designed and developed an improved in-line Bragg magnifier based on quasi-channel-cut germanium crystals. The improved set-up consists of four independent crystals, each using the (220) diffraction plane,

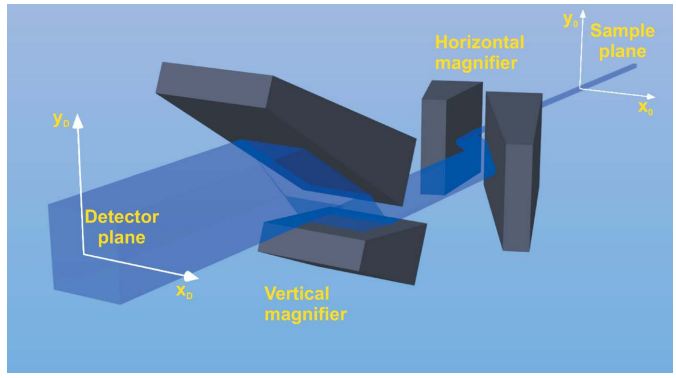


**Figure 1**
Three-dimensional model of the arrangement of the crystals forming a two-dimensional in-line Bragg magnifier.

arranged in the $\sigma(+n, -n) - \pi(+n, -n)$ configuration. This choice has several advantages over the use of a channel-cut crystal. (i) The crystal size can be easily made larger, leading to an increased field of view of the optical system. (ii) A flat crystal can be polished to a higher degree of accuracy with respect to a channel-cut crystal, which is absolutely crucial to minimize the effect on the coherence properties of the X-ray beam. (iii) Each crystal can be designed and aligned to impart the required magnification factor, to realise a uniform two-dimensional magnification. The full-field microscope is built with the crystals arranged in crossed configuration. A three-dimensional model of the optical set-up is shown in Fig. 1. The optical design allowed a 250-fold magnification to be obtained. The crystals have been prepared in the optical workshop of the European Synchrotron Radiation Facility (Grenoble, France) using a planar polishing technology (Barrett *et al.*, 2010). On the other hand, the use of independent crystals imposes more stringent requirements on the mechanical housing and the use of a more accurate alignment system. The adjustment of the diffraction planes in each quasi-channel-cut crystal is made with three piezo-driven motors.

The above-mentioned modifications make the set-up suitable for real-time X-ray imaging with high spatial resolution, estimated to be below 0.5 µm with the Medipix detector having 55 µm pixel size. The spatial resolution is limited by the numerical aperture of the Bragg magnifier (input angular acceptances) and the used experimental geometry (source size, source-to-sample and sample-to-magnifier distances). The blur caused by the penetration of X-rays into the crystals, as shown by Vagovič *et al.* (2011), in the case of extreme asymmetric cases is very small, below the resolution limit of the Bragg magnifier given by its numerical aperture, and therefore it does not limit the spatial resolution.

### 2.1. Device parameters

The asymmetry angles $\alpha_1$ and $\alpha_2$ of the first and second crystal forming the quasi-channel-cut have been specified to reach a 250-fold magnification at an X-ray energy of 11 keV. Such a value is the energy for which the angular acceptance of the system is maximized. In this sense we speak about the

**Table 1**
Main parameters of the in-line Bragg magnifier. $m_{opt}$ is the magnification at optimum energy of 11 keV, $\Delta\theta_{opt}$ is the angular acceptance and $\Delta x_{res}$ is the corresponding spatial resolution limit.

| $\alpha_1$ (°) | $\alpha_2$ (°) | $m_{opt}$ | $\Delta\theta_{opt}$ (arcsec) | $\Delta x_{res}$ (μm) |
|---|---|---|---|---|
| 16.15 | 7.04 | 250 | 66 | 0.35 |

optimal energy. As discussed in the preceding sections, such magnifications cannot be reached with a single crystal. However, using two crystals, the magnification required for the second crystal is smaller (lower asymmetry angle) than the first, the total magnification being the product of the magnification on the first and second crystal. A plot of the total magnification as a function of the incident X-ray energy is shown in Fig. 2. The main parameters are tabulated in Table 1.

The angular acceptances and the spectral bandwidth were calculated from the spectral-angular function (SAF) which is the distribution of the reflection coefficients as a function of three coordinates: input angle of the X-ray wavevector with respect to the central beam in the horizontal plane $\theta$, in the vertical plane $\varphi$ and wavelength $\lambda$ (or energy $E$) (Vagovič *et al.*, 2007). The BMM can be modeled as a $\sigma(+n, -n) - \pi(+n, -n)$ successive crystal configuration. The SAF of this system can be calculated using the two-beam dynamical theory of X-ray diffraction (Authier, 2004) employing universal computation algorithms (Huang & Dudley, 2003). The SAF is first calculated for each energy point, yielding a function of three variables $R(\theta, \varphi, E)$; then it is integrated over any two variables and the FWHM of the one-dimensional resulting function is estimated. We call these values $\Delta\theta(E)$, $\Delta\varphi(E)$ and $\Delta E(E)$. In our case, the system being symmetric in the horizontal and vertical directions, the two angular variables are equivalent. A plot of angular acceptances and bandwidth is shown in Fig. 3. The position of the maxima of the angular acceptances and bandwidth are slightly different. This means that the optimal efficiency (larger accepted bandwidth) and the optimal angular acceptance are not reached for the same energy, and a compromise is required when choosing the working parameters. We opted to design the system for optimal angular acceptance, in order to maximize the attainable spatial resolution. For illustration, the angular acceptance window of the Bragg magnifier, *i.e.* the SAF integrated over an energy range of 2 eV, is shown in Fig. 4. It is worth noting that the spectral dispersion of each quasi-channel-cut crystal is considerably large in the diffraction plane while it is rather small in the perpendicular plane. Therefore, in the crossed $\sigma$–$\pi$ configuration (the diffraction planes being perpendicular), the spectral dispersion of either channel-cut crystal in its diffraction plane is limited by the small spectral dispersion of the other one. Thus the magnifier is selecting a narrow bandwidth of about 1 eV out of a polychromatic illumination.

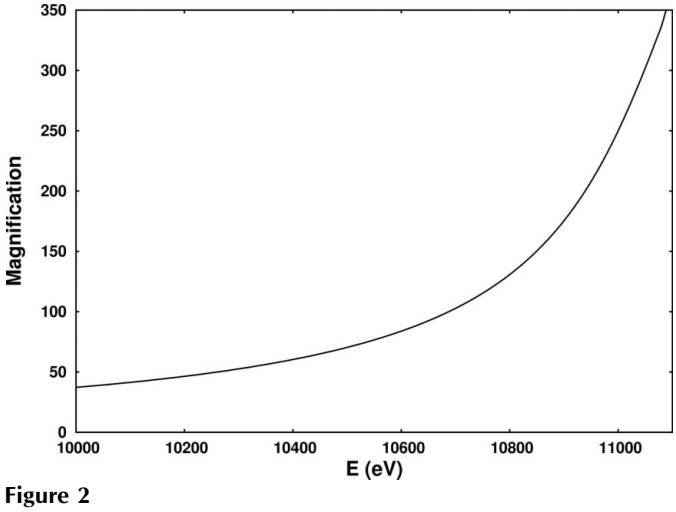


**Figure 2**
Calculated magnification of the quasi-channel-cut crystal as a function of energy.

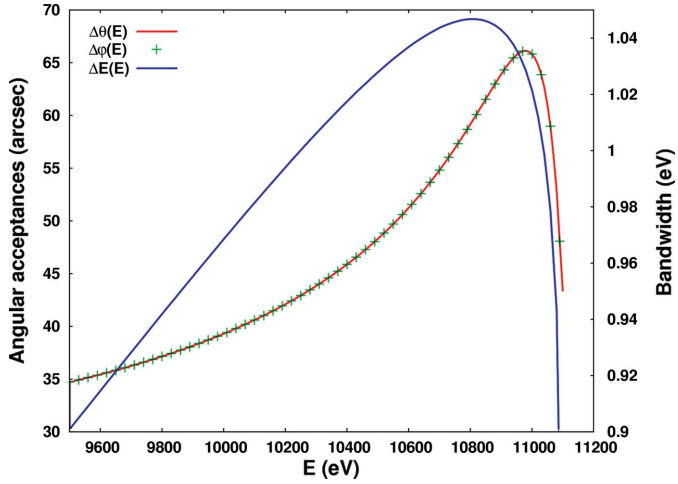


**Figure 3**
Simulation result of the estimated angular acceptances and the bandwidths as a function of the central photon energy. The simulation was performed using the spectral-angular function approach.

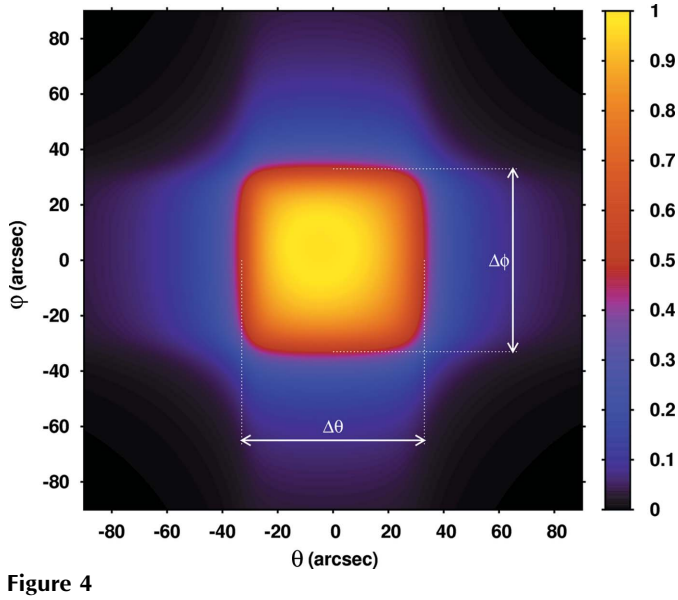


**Figure 4**
Spectral-angular function integrated over energy showing the angular input window (numerical aperture). The color scale is the normalized reflectivity coefficient.

### 2.2. Efficiency of the Bragg magnifier and Medipix detector

The efficiency of the device is a crucial parameter, especially in view of possible applications in real-time imaging with a photon-counting detector. Because the Bragg magnifier consists of perfect dislocation-free germanium crystals, one can estimate the efficiency from its SAF. We call this parameter the diffraction efficiency of the Bragg magnifier, $\eta_D$. The radiation which is transmitted through the crystal system (whose reflectivity is governed by the reflection coefficient) is then recorded by the detector. We call $\eta_C$ the detection efficiency of the detector. Finally, the efficiency of the system is defined as

$$\eta_{BMM} = \eta_D \, \eta_C. \tag{1}$$

In order to estimate the diffraction efficiency of the BMM one has to integrate the SAF over the three variables and normalize it by the integration volume as was suggested by Vagovič *et al.* (2011),

$$\eta_D = \frac{\iiint_{\Omega} R(\theta, \varphi, \lambda)\, d\theta\, d\varphi\, d\lambda}{\Omega}. \tag{2}$$

In (2), $\Omega$ is the integrating volume and $R(\theta, \varphi, \lambda)$ is the reflection coefficient of the crystal configuration given by

$$R(\theta, \varphi, \lambda) = \prod_{1}^{n} R_i(\theta, \varphi, \lambda), \qquad n = 1, 2, 3, 4, \tag{3}$$

where $n$ = 1, 2, 3, 4 is an index representing at which consecutive reflection the SAF has to be calculated. In Fig. 5 the plot of the BMM efficiency *versus* the magnification is shown, calculated for an 11 keV central photon energy. As we can see the BMM efficiency is, at first, growing with the magnification. The reason for this is the increase of the angular and spectral acceptances of the device. Finally, when the angle of input radiation is approaching the critical angle, the efficiency together with the angular and spectral acceptances are decreasing. The optimal efficiency of 4.85% is reached for a total magnification of 175. As previously explained, we designed the BMM to have 250-fold magnification at 11 keV. Therefore the diffraction efficiency is reduced to 4.10%.

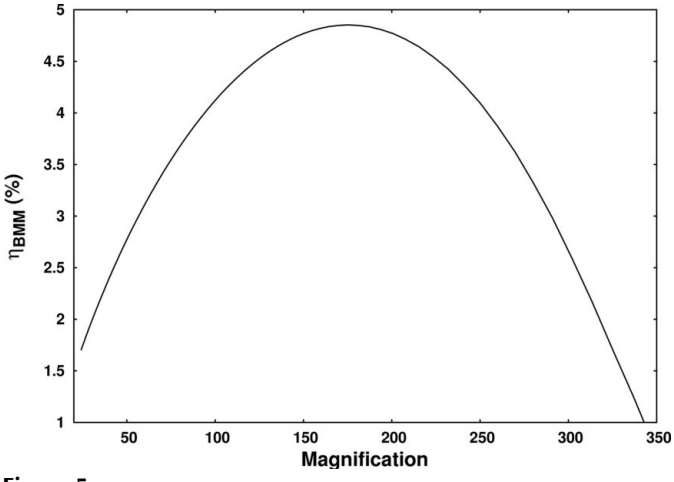


**Figure 5**
Numerical calculation of the BMM efficiency of the Bragg magnifier. For the conversion efficiency of the Medipix detector we used 100% so $\eta_{BMM} = \eta_D$. The diffraction efficiency was calculated by integrating its spectral-angular function.

## 3. Experimental tests

The BMM was experimentally tested on the TopoTomo beamline at ANKA, beamline B16 at Diamond Light Source (Sawhney *et al.*, 2010) and on the X05DA beamline at SLS (Flechsig *et al.*, 2009). A photograph of the experimental arrangement at B16 is shown in Fig. 6. The detector used was a silicon QUAD Medipix2 detector that was assembled at the National Institute for Subatomic Physics (NIKHEF, Amsterdam, The Netherlands). The sensor material thickness was equal to 300 µm with an active detector size of 28 mm × 28 mm (four Medipix readout chips in a 2 × 2 matrix) and a pixel dimension of 55 µm × 55 µm. The QUAD detector was controlled by using the *Pixelman* software package (Turecek *et al.*, 2011) and the USB interface for Medipix2 (Vykydal *et al.*, 2006).

### 3.1. Imaging performance comparison between the indirect detector and Bragg magnifier with Medipix

A comparison of the performances of the BMM with an imaging system based on a scintillator coupled to a CCD is not a straightforward task. The Medipix detector is working in single-photon-counting mode and by setting an energy threshold with essentially no dark current. The indirect detector with CCD is integrating charges and a dark current is present. To fairly compare these two systems we should proceed on a qualitative and quantitative basis. We can compare the achieved contrast (or visibility) for a given acquisition time, the signal-to-noise ratio (SNR) as a function of the acquisition time and the detected photon flux passing per unit of area through the sample per unit of time. For the illumination of the Bragg magnifier we used the radiation pre-

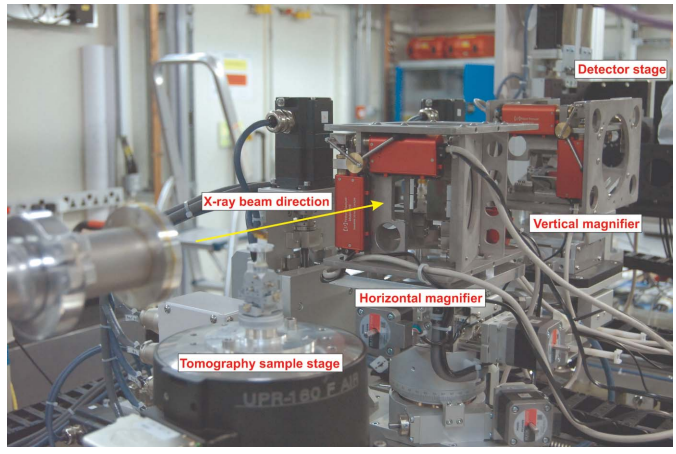


**Figure 6**
Experimental arrangement of the germanium in-line two-dimensional Bragg magnifier composed of two crossed quasi-channel-cut crystals at the Diamond B16 beamline. The mechanics for the adjustment of the quasi-channel-cut crystals was designed and manufactured by Elya Solutions s.r.o. Prague.

monochromated by a double-multilayer monochromator (DMM). Irradiation of the indirect detector system was performed using radiation delivered by a double-crystal monochromator (DCM). We consider the illumination conditions for the comparison to be correct because the Bragg magnifier itself acts as a crystal monochromator with a bandwidth of about 1 eV (see Fig. 3) which is comparable with the bandwidth of the DCM. Thus both the Medipix and the indirect detector system are illuminated with radiation of similar bandwidth. The indirect detector used was composed of (i) LAG 5 μm-thick scintillator, (ii) Optique Peter diffraction-limited microscope with available magnifications of 4, 10 and 20-fold, and (iii) CCD camera PCO4000 with a pixel size of 9 μm × 9 μm.

**3.1.1. Qualitative comparison**. For the first test, suitable for an easy comparison, we recorded the image of an X-radia X500-300-20 test pattern within 1 s using both the BMM and the indirect detector systems. The exposure time was 1 s and the X-ray energy was set to 10.6 keV. In the case of the BMM the effective pixel size was 0.39 μm and in the case of the indirect detector it was 0.45 μm, thus very similar values. The result is shown in Fig. 7. The quality of the image recorded by the BMM is significantly better while the poor SNR is the single most limiting factor for the indirect detector.

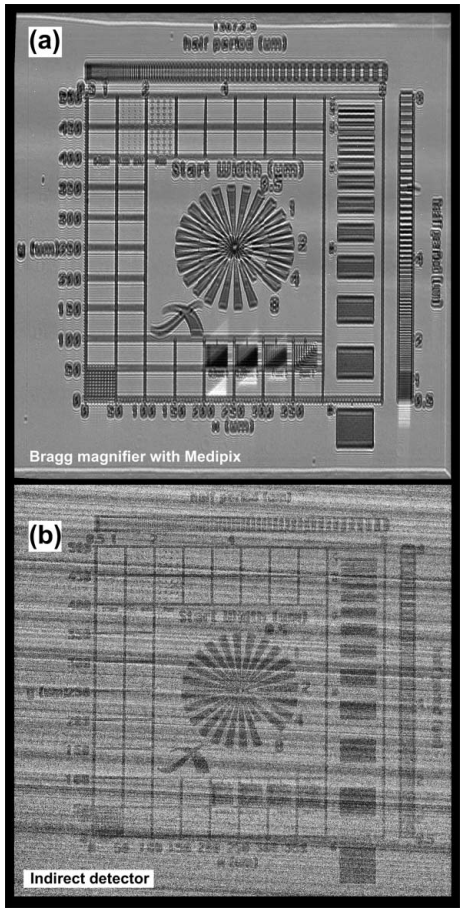


**Figure 7**
Image of an X-radia X500-300-20 test pattern recorded under similar illumination conditions with (*a*) the BMM and (*b*) the indirect detector with a magnification of 20. The significant improvement in the signal-to-noise ratio allows a better resolution to be clearly achievable.

**Table 2**
Comparison of the visibility of the intensity oscillations estimated from the intensity profile of the vertical half-period pattern of X500-300-20.

The acquisition time in the case of the indirect detector was 10 s while in the case of the BMM it was 1 s. The X-ray energy used in both cases was 10.6 keV. The effective pixel sizes were similar: 0.39 μm for the BMM and 0.45 μm for the indirect detector.

| | *V* (%) | |
|---|---|---|
| Half-period (μm) | Indirect detector | BMM |
| 0.75 | 2 | 18 |
| 1 | 8 | 30 |
| 2 | 13 | 67 |
| 4 | 22 | 56 |

Next we analysed the image contrast at selected spatial frequencies of increasing the horizontal half-pitch pattern of X500-300-20: the values are gathered in Table 2. The visibility was calculated according to $V = (I_{\max} - I_{\min})/(I_{\max} + I_{\min})$, where $I_{\max}$ and $I_{\min}$ are the maximum and minimum intensities at the given spatial frequency. For the analysis of the contrast we used an exposure time of 1 s in the case of the BMM and 10 s for the indirect detector. This choice was unavoidable in order to reach sufficient contrast to perform a meaningful visibility estimation in the latter case. As can be clearly seen, the contrast in the case of the BMM is significantly better even with a ten times shorter acquisition time.

**3.1.2. Quantitative comparison**. To compare both systems in a quantitative way we can, for example, analyse the SNR of recorded images or we can compare the flux of X-rays passing through a unit of area at the sample which is detected by the system. The second comparison will give us the information about the efficiency of both systems.

For the signal-to-noise analysis we used flat-field images recorded at an X-ray energy of 10.6 keV. The BMM was irradiated by the radiation delivered by the DMM and the indirect detector with the radiation delivered by the DCM. We calculated the signal-to-noise ratio according to following equation,

$$\mathrm{SNR} = S/\left(\sigma_{\mathrm{D}}^2 + \sigma_{\mathrm{P}}^2\right)^{1/2}, \tag{4}$$

where $S$ is the measured signal, $\sigma_{\mathrm{D}}$ is the dark noise and $\sigma_{\mathrm{P}}$ is the photonic noise. In the case of the Medipix detector the dark noise is absent. The SNR has been estimated for different exposure times and the profiles are plotted in Fig. 8 for both BMM and indirect detector. The absence of dark current greatly contributes to the better BMM performances.

To compare the detected photon flux passing through a unit area at the sample we used several magnifications for both systems. The results are shown in Fig. 9. In the case of the BMM we can see that the increase of the detected flux per unit of area towards the smaller effective pixel sizes (larger magnifications) is caused by an increase of the BMM efficiency. This is in very good agreement with the theoretical simulation, as shown in Fig. 5. In the case of the indirect

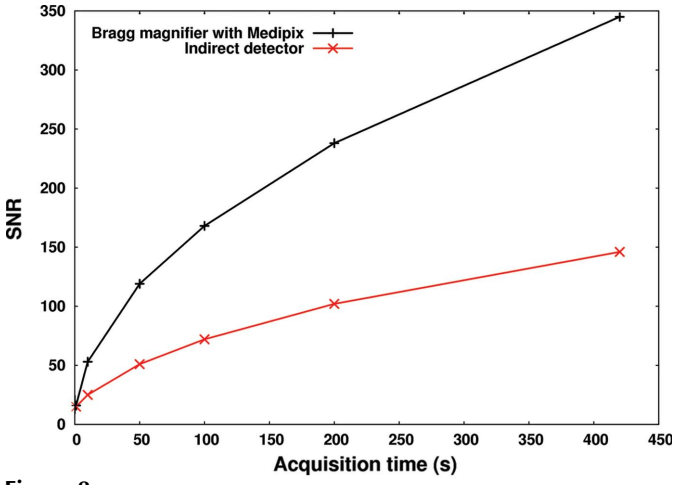


**Figure 8**
Signal-to-noise ratio for the Bragg magnifier with Medipix and for the PCO4000 with Optique Peter microscope, recorded at 10.6 keV.

detector the trend is opposite, influenced by the decrease of the SNR towards the smaller effective pixel sizes. The detected photon flux in the case of the indirect detector was calculated using the conversion efficiency equation given in Appendix A.

### 3.2. Spatial resolution estimation

Because the images are recorded in a holographic regime, the spatial resolution cannot be estimated by straightforward analysis. However, one can estimate the maximum spatial frequency for which the Fourier transform of the recorded image still displays non-negligible amplitude. For this analysis we used images recorded at 10.7 keV. For practical reasons we stayed at 10.7 keV because for higher energies the field of view was very small (<200 µm). The spatial resolution at 10.7 keV estimated by the Fourier analysis was 0.75 µm (Fig. 10).

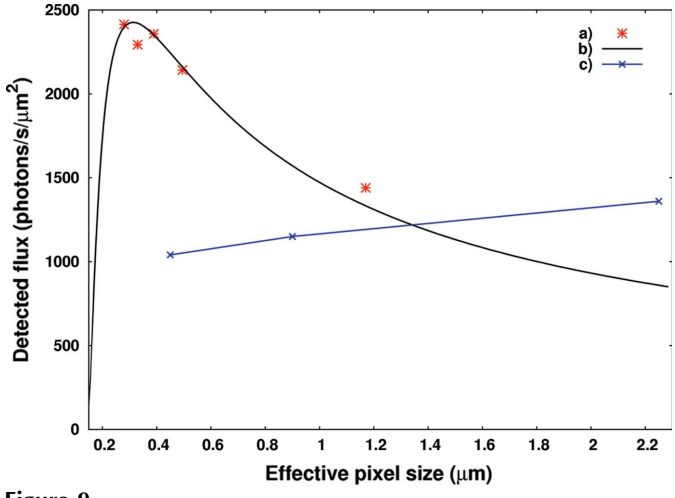


**Figure 9**
Comparison of the flux (photons $s^{-1}$ $\mu m^{-2}$) detected by the BMM (*a*) and indirect detector (*c*). Curve (*b*) is calculated by multiplying the efficiency $\eta_{BMM}$ curve (Fig. 5) by the input photon flux of $50 \times 10^3$ photons $s^{-1}$ $\mu m^{-2}$.

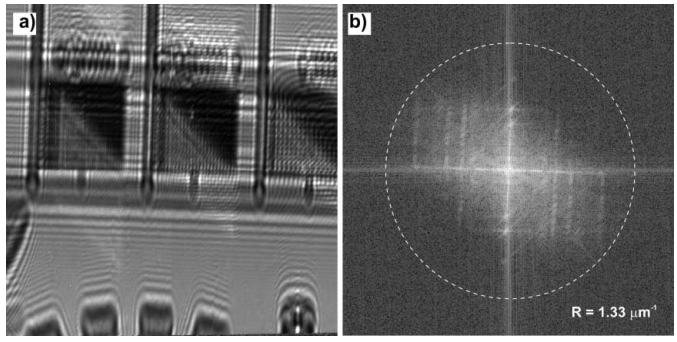


**Figure 10**
(*a*) Hologram of part of the X-radia X500-300-20 test pattern and (*b*) the amplitude of its Fourier transform. The circle with a radius of 1.33 $\mu m^{-1}$ indicates the maximum frequency still visible.

## 4. Imaging examples

As mentioned above, we address the capability of our set-up for coherent full-field imaging schemes. We report the image of weakly absorbing PMMA spheres on SiN membrane, recorded in the holographic regime (Fig. 11*a*). Being able to record holograms enables the phase shift introduced by the sample to be retrieved (if the field of view is coherently illuminated). This can be done, for example, by adopting iterative phase-retrieval algorithms from coherent diffraction imaging (Miao *et al.*, 1999). To demonstrate this approach we modified

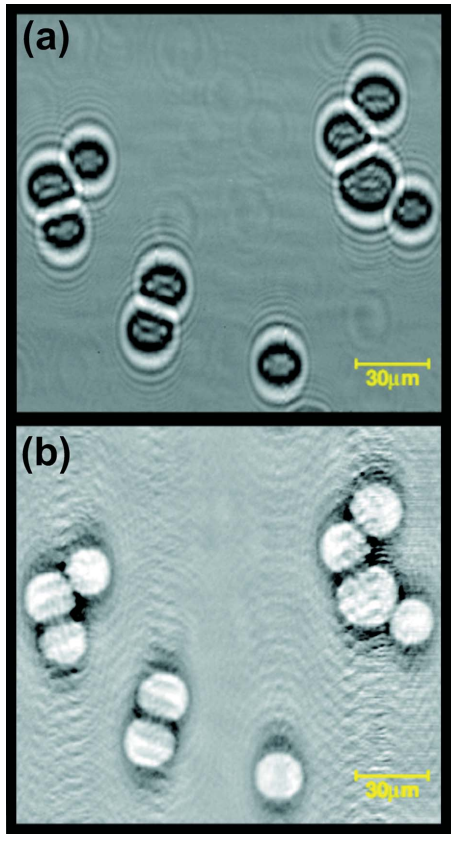


**Figure 11**
Hologram of PMMA spheres (*a*) and the retrieved phase map (*b*), recorded at 10.65 keV with 166-fold magnification.

the hybrid input–output algorithm (Fienup, 1982) for the Bragg magnifier and applied it to the phase reconstruction of the image of PMMA spheres. The image (Fig. 11*b*) shows the preliminary result (still containing some reconstruction artefacts) of the retrieved phase map. The development of the algorithm is in progress and its description will be given in a future work.

## 5. Conclusions

We have shown the performance of a novel X-ray imaging system based on a Bragg magnifier and Medipix. The results demonstrate that this system can be used for high-resolution hard X-ray holography. The performances of the system have been compared with those of a high-resolution indirect detection system. The achieved results show a clear advantage in using an X-ray magnifying system combined with single-photon-counting detectors. Compared with an indirect detector, our system has better spatial resolution, significantly higher signal-to-noise ratio and sensitivity. The optimal working resolution range of this system is between $\sim$0.4 µm and 1 µm, filling the gap between transmission X-ray microscopes and indirect detectors. The application of this system is suggested in the quantitative three-dimensional (spatial) and four-dimensional (space and time) imaging of biological and other weakly absorbing specimens with typical sizes in the range 100–500 µm.

## APPENDIX *A*
## Conversion efficiency of the indirect detector

An indirect detector is based on a luminescent screen (scintillator) which converts the X-ray image into a visible-light image. Then, the visible-light image is projected onto a CCD detector through a diffraction-limited magnifying optics. Taking into account the different steps of the image formation, the signal detected in a CCD pixel is given by the following expression,

$$S = \Phi\, E\, \eta_{\rm abs}\, {\rm LY}\, \eta_{\rm Coll}\, {\rm QE}\, {\rm ADU}, \qquad (5)$$

where $\Phi$ is the X-ray flux per unit of time and area, $E$ is the energy of X-rays (keV), $\eta_{\rm abs}$ is the X-ray absorption efficiency of the scintillator, LY is the scintillator light yield (photons keV$^{-1}$), $\eta_{\rm Coll}$ is the collection efficiency of the magnifying optics given by $({\rm NA}/n)^2/4$, where NA is the numerical aperture and $n$ is the index of refraction, QE is the quantum efficiency of the CCD detector and ADU is the analog-to-digital unit of the CCD detector.

We would like to acknowledge Andrew Malandain for his great technical support at the Diamond B16 beamline, Daniel Gauder and Julian Schäfer for production of mounting adapters, and David Haas for his outstanding IT support. DK acknowledges the support of the Scientific Grant Agency of the Ministry of Education of Slovak Republic and the Slovak Academy of Sciences No. VEGA-2/0153/10 and by the Grant of Science and Technology Assistance Agency, project No. APVV-0308-11. DP gratefully acknowledges funding from the Australian Research Council and PO acknowledges MPO CR (FR-TI1/421) for financial support.

## References

Authier, A. (2004). *Dynamical Theory of X-ray Diffraction.* Oxford University Press.
Baez, A. V. (1960). *Nature (London)*, **186**, 958.
Barrett, R., Härtwig, J., Morawe, C., Rommeveaux, A. & Snigirev, A. (2010). *Synchrotron Radiat. News*, **23**, 36–42.
Boettinger, W. J., Burdette, H. E. & Kuriyama, M. (1979). *Rev. Sci. Instrum.* **50**, 26.
Bonse, U. & Busch, F. (1996). *Prog. Biophys. Mol. Biol.* **65**, 133–169.
Cecilia, A., Rack, A., Douissard, P., Martin, T., dos Santos Rolo, T., Vagovič, P., Hamann, E., van de Kamp, T., Riedel, A., Fiederle, M. & Baumbach, T. (2011). *Nucl. Instrum. Methods Phys. Res. A*, **648**, S321–S323.
Fienup, J. R. (1982). *Appl. Opt.* **21**, 2758–2769.
Flechsig, U., Jaggi, A., Spielmann, S., Padmore, H. A. & MacDowell, A. A. (2009). *Nucl. Instrum. Methods Phys. Res. A*, **609**, 281–285.
Huang, X. & Dudley, M. (2003). *Acta Cryst.* A**59**, 163–167.
Kagoshima, Y., Tsusaka, Y., Yokoyama, K., Takai, K., Takeda, S., Kobayashi, K., Kimura, H., Kimura, S. & Izumi, K. (2000). *AIP Conf. Proc.* **507**, 41–44.
Kirkpatrick, P. & Baez, A. V. (1948). *J. Opt. Soc. Am.* **38**, 766–774.
Kobayashi, K., Izumi, K., Kimura, H., Kimura, S., Ibuki, T., Yokoyama, Y., Tsusaka, Y., Kagoshima, Y. & Matsui, J. (2001). *Appl. Phys. Lett.* **78**, 132–134.
Llopart, X., Campbell, M., Dinapoli, R., San Segundo, D. & Pernigotti, E. (2002). *IEEE Trans. Nucl. Sci.* **49**, 2279–2283.
Miao, J., Charalambous, P., Kirz, J. & Sayre, D. (1999). *Nature (London)*, **400**, 342–344.
Pelliccia, D., Sorrentino, A., Bukreeva, I., Cedola, A., Scarinci, F., Ilie, M., Gerardino, A. M., Fratini, M. & Lagomarsino, S. (2010). *Opt. Express*, **18**, 15998–16004.
Sawhney, K., Dolbnya, I., Tiwari, M., Alianelli, L., Scott, S., Preece, G., Pedersen, U. & Walton, R. (2010). *AIP Conf. Proc.* **1234**, 387.
Schäfer, P. & Köhler, R. (2003). *J. Phys. D*, **36**, A113–A117.
Spal, R. D. (2001). *Phys. Rev. Lett.* **14**, 3044–3047.
Stampanoni, M., Borchert, G. & Abela, R. (2006). *Radiat. Phys. Chem.* **75**, 1956–1961.
Stampanoni, M., Borchert, G., Abela, R. & Rüegsegger, P. (2002). *J. Appl. Phys.* **92**, 7630–7635.
Suehiro, S., Miyaji, H. & Hayashi, H. (1991). *Nature (London)*, **352**, 385–386.
Turecek, D., Holy, T., Jakubek, J., Pospisil, S. & Vykydal, Z. (2011). *J. Instrum.* **6**, C01046.
Vagovič, P., Korytár, D., Mikulík, P., Cecilia, A., Ferrari, C., Yang, Y., Hänschke, D., Hamann, E., Pelliccia, D., Lafford, T. A., Fiederle, M. & Baumbach, T. (2011). *J. Synchrotron Rad.* **18**, 753–760.
Vagovič, P., Korytár, D., Mikulík, P. & Ferrari, C. (2007). *Nucl. Instrum. Methods Phys. Res. B*, **265**, 599–604.
Vykydal, Z., Jakubek, J. & Pospisil, S. (2006). *Nucl. Instrum. Methods Phys. Res. A*, **563**, 112–115.